

# Local and Multi-Scale Strategies to Mitigate Exponential Concentration in Quantum Kernels

Claudia Zendesas-Morales  
University of Copenhagen, Denmark

Debashis Saikia  
Indian Institute of Science Education and Research, Thiruvananthapuram

Utkarsh Singh  
Department of Physics, University of Ottawa, 25 Templeton Street, Ottawa, Ontario, K1N 6N5 Canada and  
National Research Council of Canada, 100 Sussex Drive, Ottawa, Ontario K1N 5A2, Canada

Fidelity-based quantum kernels provide a direct interface between quantum feature maps and classical kernel methods, but they can exhibit exponential concentration: with increasing system size or circuit expressivity, the Gram matrix approaches the identity and suppresses informative similarity structure. We present an empirical study of two mitigation strategies implemented in Qiskit: (i) *local* (patch-wise) kernels that aggregate subsystem similarities, and (ii) *multi-scale* kernels that mix local and global similarity across patch granularities.

We benchmark baseline, local, and multi-scale kernels under matched preprocessing, splits, and SVM protocols on several tabular datasets, sweeping the feature dimension  $d \in \{4, 6, \dots, 20\}$ . We report concentration diagnostics based on off-diagonal kernel statistics, spectral richness via effective rank, and centered alignment with labels. Across datasets, local and multi-scale constructions consistently mitigate concentration and yield richer kernel spectra relative to the global fidelity baseline, while the impact on classification accuracy depends on the dataset and dimension.

## I. INTRODUCTION

Kernel methods are a standard approach to nonlinear learning that separates representation from optimization. Given training data  $\{\mathbf{x}_i\}_{i=1}^n \subset \mathbb{R}^d$ , a positive semidefinite kernel  $k: \mathbb{R}^d \times \mathbb{R}^d \rightarrow \mathbb{R}$  defines a Gram matrix  $K \in \mathbb{R}^{n \times n}$ , with entries

$$K_{ij} = k(\mathbf{x}_i, \mathbf{x}_j). \quad (1)$$

Classical algorithms such as support vector machines can then be trained using  $K$  [1].

Quantum kernel methods instantiate  $k$  using a quantum feature map. A parameterized circuit  $U_\phi(\mathbf{x})$  prepares an encoded state

$$|\psi(\mathbf{x})\rangle = U_\phi(\mathbf{x})|0\rangle^{\otimes d}, \quad (2)$$

Here,  $\phi$  denotes the feature map implemented by the circuit family  $U_\phi$ , and  $|\psi(\mathbf{x})\rangle$  denotes the corresponding encoded quantum state. The choice of data encoding (feature map) critically shapes the induced kernel and, consequently, the expressivity and generalization behavior of the resulting quantum model [2]. A common choice of kernel is the squared fidelity

$$k_{\text{fid}}(\mathbf{x}, \mathbf{x}') = |\langle \psi(\mathbf{x}) | \psi(\mathbf{x}') \rangle|^2. \quad (3)$$

This approach is attractive in the noisy intermediate-scale quantum regime because the optimization problem remains classical while the quantum device provides a structured, potentially high-dimensional embedding [3–6].

A central obstacle for fidelity-based quantum kernels is *exponential concentration*. Empirically and theoretically, as the number of qubits and or circuit expressivity increase, overlaps between distinct encoded states can concentrate around

a data-independent value.[7–9] In the regime where feature-map states resemble random states, off-diagonal entries of  $K$  become small and the Gram matrix approaches a low-variance form. This collapse can suppress label-relevant structure and can make reliable estimation of  $k_{\text{fid}}(\mathbf{x}, \mathbf{x}')$  shot-expensive [7]. For kernel methods, concentration is therefore both a statistical issue (loss of informative variation across  $K$ ) and an operational issue (measurement cost).

Related work has highlighted both the promise and limitations of quantum kernels. Early demonstrations of quantum-enhanced feature spaces focused on fidelity-style kernels induced by parametric circuits [3, 4]. Subsequent analyses emphasized that the apparent expressivity of large Hilbert spaces does not by itself guarantee learnability or generalization, and that kernel quality depends on data, encoding, and measurement choices [7, 10]. Our contribution is positioned as a practical study of two mitigation strategies that modify the similarity statistic itself through locality and scale mixing, and we evaluate these strategies with matched protocols across increasing feature dimension.

This work studies two practical strategies to mitigate the reliance on a single global overlap. The first strategy constructs *local* (patch-wise) kernels by evaluating similarity on small subsystems and aggregating the results. Let  $\mathcal{P} = \{P_1, \dots, P_M\}$  be a collection of patches (subsets of qubits). For each patch  $P_m$  we form the reduced state

$$\rho^{(P_m)}(\mathbf{x}) = \text{Tr}_{\overline{P_m}}(|\psi(\mathbf{x})\rangle \langle \psi(\mathbf{x})|), \quad (4)$$

and define a patch kernel, for example via the Hilbert–Schmidt inner product

$$\kappa_{P_m}(\mathbf{x}, \mathbf{x}') = \text{Tr}(\rho^{(P_m)}(\mathbf{x}) \rho^{(P_m)}(\mathbf{x}')). \quad (5)$$

The local kernel is obtained by a convex aggregation,

$$k_{\text{loc}}(\mathbf{x}, \mathbf{x}') = \sum_{m=1}^M w_m \kappa_{P_m}(\mathbf{x}, \mathbf{x}'), \quad w_m \geq 0, \quad \sum_{m=1}^M w_m = 1. \quad (6)$$

The second strategy constructs *multi-scale kernels* by combining kernels computed at multiple patch granularities. Given a set of scales  $\{\mathcal{P}^{(s)}\}_{s=1}^S$ , we build one kernel per scale and define the multi-scale kernel function as a convex combination

$$k_{\text{ms}}(\mathbf{x}, \mathbf{x}') = \sum_{s=1}^S \alpha_s k^{(s)}(\mathbf{x}, \mathbf{x}'), \quad \alpha_s \geq 0, \quad \sum_{s=1}^S \alpha_s = 1. \quad (7)$$

Here,  $k^{(s)}$  denotes the kernel induced by scale  $\mathcal{P}^{(s)}$ . Locality reduces sensitivity to global scrambling, while multi-scale mixing aims to preserve information that may appear at different subsystem sizes.

Our study is intentionally empirical and reproducible. We implement baseline (global), local, and multi-scale kernels in Qiskit under a unified API and benchmark them with matched experimental protocols over feature dimension  $d \in \{4, 6, \dots, 20\}$ . To quantify kernel concentration and its downstream impact, we report off-diagonal summary statistics, effective rank as a proxy for spectral richness, and centered alignment with labels, along with support vector machine (SVM) performance using precomputed kernels. Across the datasets we consider, local and multi-scale constructions consistently reshape kernel geometry relative to the baseline fidelity kernel, while improvements in accuracy remain dataset dependent.

**Contributions and organization.** We provide (i) Qiskit implementations of baseline, local, and multi-scale quantum kernels under a unified API, (ii) a reproducible benchmark pipeline with fixed preprocessing, splits, and hyperparameter policies, and (iii) diagnostics that quantify concentration and downstream performance across a feature-dimension sweep. The remainder of this paper is organized as follows. Section II describes the kernel constructions, feature maps, datasets, and evaluation protocol. Section III presents experimental results and diagnostic analyses. Code and configuration files to reproduce the experiments and figures are available in the accompanying repository.

## II. METHODS

### A. Kernel definitions

Throughout, we represent a classical input as a feature vector  $\mathbf{x} \in \mathbb{R}^d$ . For a dataset  $\{\mathbf{x}_i\}_{i=1}^n$ , a kernel function  $k(\cdot, \cdot)$  induces a Gram matrix  $K \in \mathbb{R}^{n \times n}$  with entries  $K_{ij} = k(\mathbf{x}_i, \mathbf{x}_j)$  as in Eq. (1). The corresponding encoded quantum state  $|\psi(\mathbf{x})\rangle$  is prepared by applying the feature-map circuit  $U_\phi(\mathbf{x})$  as in Eq. (2).

### 1. Baseline (global fidelity) kernel

The baseline kernel is the global fidelity kernel defined in Eq. (3). Operationally, we compute it by first preparing the statevector for each sample,

$$\mathbf{s}_i \equiv |\psi(\mathbf{x}_i)\rangle \in \mathbb{C}^{2^d}, \quad (8)$$

then forming the overlap matrix

$$G_{ij} = \langle \psi(\mathbf{x}_i) | \psi(\mathbf{x}_j) \rangle, \quad G = SS^\dagger, \quad (9)$$

where  $S \in \mathbb{C}^{n \times 2^d}$  is the matrix whose  $i$ th row is  $\mathbf{s}_i^\top$  (equivalently,  $S = [\mathbf{s}_1^\top; \dots; \mathbf{s}_n^\top]$ ). Finally, the Gram matrix is given entrywise by

$$K_{ij}^{\text{fid}} = |G_{ij}|^2. \quad (10)$$

In our implementation we symmetrize  $K^{\text{fid}}$  by replacing it with  $(K^{\text{fid}} + (K^{\text{fid}})^\top)/2$  and set the diagonal entries to 1. The symmetrization enforces the exact symmetry that holds in the ideal definition, but that may be violated slightly by finite-precision arithmetic; this improves numerical stability for downstream operations such as spectral decompositions. Setting  $K_{ii}^{\text{fid}} = 1$  enforces the exact self-similarity  $|\langle \psi(\mathbf{x}_i) | \psi(\mathbf{x}_i) \rangle|^2 = 1$ , which can otherwise deviate from unity at the level of floating-point error.

### 2. Local (patch-wise) kernels

The motivation for locality is that exponential concentration of the global fidelity kernel is driven by a single overlap of  $d$ -qubit states, which can become nearly constant (and typically small) for most distinct inputs as circuit expressivity grows. By instead evaluating similarities on small subsystems and aggregating them, local kernels probe overlaps in smaller effective Hilbert spaces and are less sensitive to global scrambling. As a result, the aggregated Gram matrix can retain richer off-diagonal variation than the baseline fidelity kernel while still defining a valid similarity measure.

Let  $\mathcal{P} = \{P_1, \dots, P_M\}$  be a collection of patches, where each patch  $P_m \subseteq \{0, 1, \dots, d-1\}$  indexes a subset of qubits. When not specified otherwise, we use the default disjoint partition into adjacent pairs  $P_m = (2m, 2m+1)$ . When specified partitions are provided, we set  $\mathcal{P}$  equal to that collection of index sets and apply the same patch-kernel construction and aggregation without further modification. For completeness, Algorithm 1 in Appendix A summarizes the end-to-end procedure we use to construct the local (patch-wise) kernel.

We support two implementations for computing patch-wise similarities (followed by a common aggregation step).

*a. Subcircuit-based patch kernel.* For each patch  $P_m$ , we construct a feature-map circuit restricted to the qubits in  $P_m$  and use the corresponding feature subvector  $\mathbf{x}_{P_m}$  obtained by selecting the components of  $\mathbf{x}$  indexed by  $P_m$ . Denoting the resulting patch state by  $|\psi_{P_m}(\mathbf{x})\rangle$ , the patch kernel is

$$k_{\text{sub}}^{(P_m)}(\mathbf{x}, \mathbf{x}') = |\langle \psi_{P_m}(\mathbf{x}) | \psi_{P_m}(\mathbf{x}') \rangle|^2. \quad (11)$$

*b. Reduced Density Matrix (RDM) local kernel.* Alternatively, we prepare the full  $d$ -qubit state  $|\psi(\mathbf{x})\rangle$  and compute the reduced density matrix on a patch by tracing out the complement,

$$\rho^{(P_m)}(\mathbf{x}) = \text{Tr}_{\overline{P_m}}(|\psi(\mathbf{x})\rangle\langle\psi(\mathbf{x})|). \quad (12)$$

Here,  $\overline{P_m}$  denotes the set of qubits not contained in  $P_m$  (i.e., the complement of  $P_m$  in  $\{0, 1, \dots, d-1\}$ ). We then define the patch similarity using either the quantum state fidelity  $F\left(\rho^{(P_m)}(\mathbf{x}), \rho^{(P_m)}(\mathbf{x}')\right)$  or the Hilbert–Schmidt inner product  $\text{Tr}\left(\rho^{(P_m)}(\mathbf{x})\rho^{(P_m)}(\mathbf{x}')\right)$ .

*c. Patch aggregation.* Patch kernels are aggregated by either an unweighted mean or a weighted mean. In the unweighted case, the arithmetic mean corresponds to using uniform weights  $w_m = 1/M$ . With weights  $w_m \geq 0$  and  $\sum_{m=1}^M w_m = 1$ , the aggregated local kernel is

$$k_{\text{loc}}(\mathbf{x}, \mathbf{x}') = \sum_{m=1}^M w_m k^{(P_m)}(\mathbf{x}, \mathbf{x}'). \quad (13)$$

### 3. Multi-scale kernels

A multi-scale kernel combines kernels computed at multiple granularities. The motivation is that relevant structure may appear at different subsystem sizes: small patches can capture short-range correlations, while larger patches can capture more global similarity. By mixing multiple patch granularities, the kernel can reduce reliance on a single highly concentrated global overlap while retaining informative similarities at intermediate scales.

We specify a collection of scales  $\{\mathcal{P}^{(s)}\}_{s=1}^S$ , where each scale  $\mathcal{P}^{(s)}$  is itself a set of patches. For each scale, we compute a per-scale kernel by averaging the corresponding patch similarities. When a patch contains all qubits, the patch contribution is computed as a fidelity kernel; otherwise it is computed as a Hilbert–Schmidt inner product between patch RDMs. The final multi-scale kernel is a convex combination

$$k_{\text{ms}}(\mathbf{x}, \mathbf{x}') = \sum_{s=1}^S \alpha_s k^{(s)}(\mathbf{x}, \mathbf{x}'), \quad \alpha_s \geq 0, \quad \sum_{s=1}^S \alpha_s = 1. \quad (14)$$

where the weights  $\{\alpha_s\}$  are renormalized to sum to one. Unless specified otherwise, we use uniform scale weights (i.e.,  $\alpha_s = 1/S$ ); in particular, for the default two-scale construction we use  $\alpha_1 = \alpha_2 = 1/2$ . When scales are not specified, we use a default two-scale construction consisting of (i) disjoint adjacent pairs and (ii) the full system. In our implementation, we compute one kernel per scale by averaging patch contributions, then combine the per-scale kernels with nonnegative weights that are renormalized to sum to one. For patches smaller than the full system we use the Hilbert–Schmidt inner product between patch reduced density matrices, while for the full-system patch we use the state fidelity. Finally, unless otherwise specified, we normalize the resulting multi-scale Gram matrix to have unit diagonal and enforce exact symmetry. For

completeness, Algorithm 2 in Appendix B summarizes the end-to-end procedure we use to construct the multi-scale kernel.

### 4. Normalization and PSD correction

Kernel matrices computed from finite-precision statevector arithmetic can exhibit small asymmetries and, in some cases, tiny negative eigenvalues that are numerical artifacts rather than physical effects. To make kernels comparable across feature dimensions and constructions, we enforce a common *unit-diagonal normalization*. For any kernel matrix  $K$  with nonnegative diagonal, we apply

$$K_{ij} \leftarrow \frac{K_{ij}}{\sqrt{K_{ii}K_{jj}}}, \quad (15)$$

which rescales the kernel so that  $K_{ii} = 1$  for all samples.

In addition, we explicitly symmetrize the numerically computed Gram matrices via  $K \leftarrow (K + K^\top)/2$ .

*a. Local kernel.* For the local (patch-wise) kernel, we further apply a positive-semidefinite (PSD) correction after aggregation by projecting onto the PSD cone using eigenvalue clipping. Concretely, for the eigendecomposition  $K = V \text{diag}(\lambda) V^\top$ , we set negative eigenvalues below a small threshold to zero and reconstruct  $K$ . We then reapply the unit-diagonal normalization.

*b. Baseline and multi-scale kernels.* For the baseline fidelity kernel and the multi-scale kernel, our implementation enforces symmetry and a unit diagonal but does not perform an explicit PSD projection; in practice, any observed PSD violations in these constructions are typically at the level of numerical noise.

## B. Feature maps and implementation

*a. ZZ-style feature maps.* All quantum kernels in this work are instantiated using ZZ-style data-encoding circuits that map an input feature vector  $\mathbf{x} \in \mathbb{R}^d$  to a  $d$ -qubit state  $|\psi(\mathbf{x})\rangle$ . We implement three closely related variants (selected via a unified API): (i) a simple *manual ZZ*-style map (`zz_manual`) based on single-qubit  $R_x$  rotations followed by *CZ* entangling gates; (ii) a more *canonical-like manual ZZ* map (`zz_manual_canonical`) based on an initial layer of Hadamards followed by repeated layers of local  $R_z$  rotations and pairwise  $R_{ZZ}$  interactions; and (iii) Qiskit’s circuit-library implementation (`zz_qiskit`) based on `qiskit.circuit.library.zz_feature_map`.

*b. Depth and entanglement patterns.* We denote the number of repetitions (layers) of the feature map by  $L$  (depth in the code). Unless otherwise specified, we use shallow feature maps (typically  $L = 1$ ) to enable matched sweeps over feature dimension  $d \in \{4, 6, \dots, 20\}$ . For the manual feature maps, we use `linear` and `ring` entanglement patterns (nearest-neighbor couplings, with `ring` additionally coupling the last and first qubits). For the Qiskit feature map, we use

entanglement patterns supported by the library implementation (we use `linear` in our main sweeps).

*c. Statevector backend.* All kernel matrices reported in this paper are computed using exact statevector simulation in Qiskit [11]. Concretely, each kernel implementation constructs the feature-map circuit for each sample and evaluates state overlaps (baseline and full-patch contributions) via inner products of statevectors. Local and multi-scale kernels compute patch reduced density matrices using partial traces on the statevector and then evaluate patch similarities.

*d. Kernel post-processing: symmetry, normalization, and centering.* Across kernel families we apply consistent numerical post-processing. First, we explicitly enforce symmetry via  $K \leftarrow (K + K^\top)/2$ . Second, we apply unit-diagonal normalization as in Eq. (15). For the local kernel only, we additionally apply eigenvalue clipping to enforce positive semidefiniteness, followed by a second unit-diagonal normalization.

Some experiments and diagnostics use *centered* kernels. Given a Gram matrix  $K \in \mathbb{R}^{n \times n}$ , we center it as  $K_c = HKH$  with  $H = I - \frac{1}{n}\mathbf{1}\mathbf{1}^\top$ . Unless otherwise specified, we report results for uncentered kernels and compute centered alignment with labels as a diagnostic.

### C. Datasets and preprocessing

*a. Datasets.* We evaluate on a mixture of synthetic and real-world datasets, using a common pipeline that produces matched train/validation/test splits and precomputed-kernel SVM evaluation. The main experiments focus on real tabular datasets: `breast_cancer` (via `sklearn.datasets.load_breast_cancer`) [12], `parkinsons` (via `sklearn.datasets.fetch_openml` with `data_id=1488`) [13], `ionosphere` [14], `heart_disease` [15], and subset runs for larger datasets such as `exam_score_prediction` [16] and `star_classification` [17].

*b. Scaling and angle encoding.* All datasets are standardized prior to quantum embedding. After scaling, each feature is treated as a rotation angle and passed directly to the selected ZZ-style feature map, so that the feature dimension equals the number of qubits ( $d$ ).

*c. Target feature dimensions*  $d \in \{4, 6, \dots, 20\}$ . To study concentration as a function of system size, we evaluate each dataset at a common set of feature dimensions  $d \in \{4, 6, \dots, 20\}$ . When a dataset has more than  $d$  available features, we reduce to the target dimension using PCA. When a dataset has fewer raw features than required for the sweep, we augment it with simple engineered features based on pairwise interactions (products) to reach the desired dimension while keeping the protocol consistent across kernels.

*d. Splits and random seeds.* For each dataset and target dimension  $d$ , we use deterministic train/validation/test splits controlled by a fixed random seed. To assess stability, experiments can be repeated over multiple seeds, and all kernels (baseline, local, and multi-scale) are evaluated using a controlled protocol (same splits, preprocessing, and hyperparameters). All split indices and labels are saved alongside each

kernel matrix for reproducibility.

### D. Scalability: Nyström approximation (optional)

Computing full kernel matrices scales quadratically in the number of samples ( $O(n^2)$ ) and can become a bottleneck for larger datasets. As an optional scalability mechanism, our codebase supports a Nyström/landmark approximation, which approximates the full Gram matrix using a smaller set of  $m \ll n$  landmark points [18].

*a. Approximation.* Let  $X = \{\mathbf{x}_i\}_{i=1}^n$  be the full dataset and let  $Z = \{\mathbf{z}_j\}_{j=1}^m \subset X$  denote a subset of landmark points. Define the cross-kernel matrix  $C \in \mathbb{R}^{n \times m}$  with entries  $C_{ij} = k(\mathbf{x}_i, \mathbf{z}_j)$  and the landmark Gram matrix  $W \in \mathbb{R}^{m \times m}$  with entries  $W_{ij} = k(\mathbf{z}_i, \mathbf{z}_j)$ . The Nyström approximation of the full kernel is then

$$\tilde{K} = CW^\dagger C^\top, \quad (16)$$

where  $W^\dagger$  denotes the (pseudo-)inverse of  $W$ . Equivalently, one can form an explicit feature representation  $\Phi = CW^{-1/2}$  and train a linear model on  $\Phi$ .

*b. Implementation details.* We implement Nyström support by providing cross-kernel computation routines for each kernel family. These routines compute the cross-kernel  $C = K(X, Z)$  between a set of samples and a set of landmark points, optionally using chunking to avoid large intermediate allocations, and they reuse the same patch/scale logic as the corresponding full-kernel construction. On the evaluation side, our SVM utility supports both (i) precomputed-kernel SVMs for full kernels and (ii) linear SVMs on explicit feature matrices for Nyström-style approximations.

*c. Why we include it.* Nyström provides a standard and lightweight route to scaling kernel experiments while keeping the kernel construction tied to the same underlying similarity function. In this project it primarily serves as infrastructure for future experiments on larger datasets; unless noted otherwise, the results in this paper use the exact (non-Nyström) statevector kernels.

### E. Diagnostics and evaluation

To quantify how strongly a kernel concentrates and how much information it retains for downstream learning, we report three geometry diagnostics computed from the Gram matrix  $K \in \mathbb{R}^{n \times n}$ , together with an SVM evaluation using precomputed kernels.

*a. Off-diagonal concentration (p50/p95).* Let  $\mathcal{I} = \{(i, j) : i \neq j\}$  denote the off-diagonal index set and let  $\{K_{ij}\}_{(i,j) \in \mathcal{I}}$  be the multiset of off-diagonal entries. We summarize concentration using the median (p50) and the upper-tail percentile (p95),

$$\begin{aligned} \text{p50}(K) &= \text{percentile}_{50}(\{K_{ij}\}_{i \neq j}), \\ \text{p95}(K) &= \text{percentile}_{95}(\{K_{ij}\}_{i \neq j}). \end{aligned} \quad (17)$$

As  $d$  (or circuit expressivity) increases, exponential concentration manifests as off-diagonal entries shrinking toward zero; correspondingly, both p50 and p95 decrease and the kernel approaches the identity.

*b. Effective rank (entropy-based).* To characterize spectral richness, we compute the eigenvalues of the symmetrized kernel  $K_s = \frac{1}{2}(K + K^\top)$  and denote them by  $\{\lambda_i\}_{i=1}^n$ . We clip small negative eigenvalues (numerical artifacts) to 0 and form a probability distribution  $p_i = \lambda_i / \sum_j \lambda_j$ . The entropy-based effective rank is then [19]

$$r_{\text{eff}}(K) = \exp \left( - \sum_{i=1}^n p_i \log p_i \right). \quad (18)$$

Large  $r_{\text{eff}}$  indicates a flatter spectrum and a richer kernel geometry, whereas a small  $r_{\text{eff}}$  indicates spectral collapse.

*c. Centered alignment with labels.* We compute the centered kernel alignment between  $K$  and a label kernel  $L$  [20]. Let  $H = I - \frac{1}{n}\mathbf{1}\mathbf{1}^\top$  be the centering matrix, and define centered kernels  $K_c = HKH$  and  $L_c = HLH$ . For multi-class labels  $y \in \{1, \dots, C\}^n$ , we build  $L$  from one-hot encodings  $Y \in \mathbb{R}^{n \times C}$  via  $L = YY^\top$ . The centered alignment is

$$\mathcal{A}(K, y) = \frac{\langle K_c, L_c \rangle_F}{\|K_c\|_F \|L_c\|_F}, \quad \langle A, B \rangle_F = \text{Tr}(A^\top B). \quad (19)$$

This statistic measures how well the similarity structure in  $K$  matches label similarity after removing global mean effects.

*d. SVM protocol and hyperparameter grid.* For each dataset (and each target dimension  $d$ ), we use fixed train/validation/test splits that are shared across kernel families. Given a full Gram matrix  $K$ , we train an SVM with a precomputed kernel using  $K_{\text{train}} = K[\text{train}, \text{train}]$ . For model selection, we sweep the regularization parameter  $C$  over the grid

$$\mathcal{C} = \{0.1, 1, 10\}, \quad (20)$$

choose the value maximizing validation accuracy, and then report test accuracy using the selected  $C$  on  $K_{\text{test}} = K[\text{test}, \text{train}]$ . All kernels are evaluated under the same splits and the same  $\mathcal{C}$  grid to enable matched comparisons.

### III. RESULTS AND ANALYSIS

#### A. Kernel concentration and spectral richness vs. feature dimension

We first study how kernel geometry changes as the feature dimension  $d$  increases. For each dataset we run a matched sweep over  $d \in \{4, 6, \dots, 20\}$  and compute (i) off-diagonal concentration statistics (median p50 and upper-tail p95) and (ii) spectral richness via the entropy-based effective rank  $r_{\text{eff}}$  defined in Eq. (18). All kernels are normalized to unit diagonal, so changes in p50/p95 directly reflect how much similarity mass remains in the off-diagonals as  $d$  grows. Unless otherwise noted, all curves are produced using the fixed deterministic train/validation/test split described in Section II.

*a. Off-diagonal concentration (p50).* Figure 1 shows the off-diagonal median (p50) as a function of  $d$ . Across all datasets, the baseline (global fidelity) kernel exhibits the strongest concentration signature: as  $d$  increases, the p50 curve rapidly decreases toward 0, consistent with the Gram matrix approaching the identity. In contrast, the local kernel maintains substantially higher p50 values over the same sweep, indicating that patch-wise aggregation retains nontrivial similarity structure at larger  $d$ . As expected, the multi-scale kernel typically interpolates between the baseline and local curves because it explicitly mixes global and local similarity. In most cases the baseline-local gap widens with  $d$ , highlighting that locality preserves meaningful off-diagonal similarity even in regimes where the global fidelity kernel is close to an identity matrix.

*b. Upper-tail behavior (p95).* The p95 statistic (Appendix C, Fig. 6) probes whether a small subset of pairs remains highly similar even when the median similarity collapses. We again observe a consistent ordering: baseline concentrates fastest, local concentrates slowest, and multi-scale is intermediate. Operationally, this suggests that locality mitigates not only the typical pairwise overlap (p50) but also the collapse of the similarity tail (p95), thereby preserving more heterogeneous pairwise structure.

*c. Spectral richness (effective rank).* Figure 2 reports the entropy-based effective rank of the kernel spectrum. As  $d$  increases, the baseline kernel typically shows a strong reduction in  $r_{\text{eff}}$ , reflecting spectral collapse toward a low-information geometry. Local kernels consistently maintain a richer spectrum (larger  $r_{\text{eff}}$ ), while multi-scale again tends to lie between baseline and local. In this setting, a larger  $r_{\text{eff}}$  indicates that spectral mass is spread across more directions in feature space, while a small  $r_{\text{eff}}$  indicates that the kernel is effectively close to low-rank or identity-like (few informative directions after centering/normalization). Although  $r_{\text{eff}}$  is a coarse summary, it aligns well with the concentration statistics: kernels with larger p50/p95 generally retain a flatter and more informative eigen-spectrum.

*d. Representative eigen-spectra (qualitative).* In addition to the effective-rank summary, Appendix C (Fig. 9) provides representative eigen-spectrum examples at a fixed feature dimension ( $d = 12$ ). A consistent qualitative signature is that the baseline kernel typically exhibits a noticeably steeper eigenvalue decay (more spectral mass in the leading eigenvalues), while local and multi-scale kernels distribute spectral mass more evenly; this pattern is aligned with the higher effective-rank values reported in Fig. 2.

#### B. SVM performance

We next evaluate whether the geometric changes induced by local and multi-scale kernels translate into improved downstream classification. For each dataset and dimension  $d$ , we train an SVM with a precomputed kernel on the training split. The regularization parameter  $C$  is selected by validation accuracy from the fixed grid  $\mathcal{C} = \{0.1, 1, 10\}$  (Eq. (20)) independently for each kernel family; we then report the correspond-

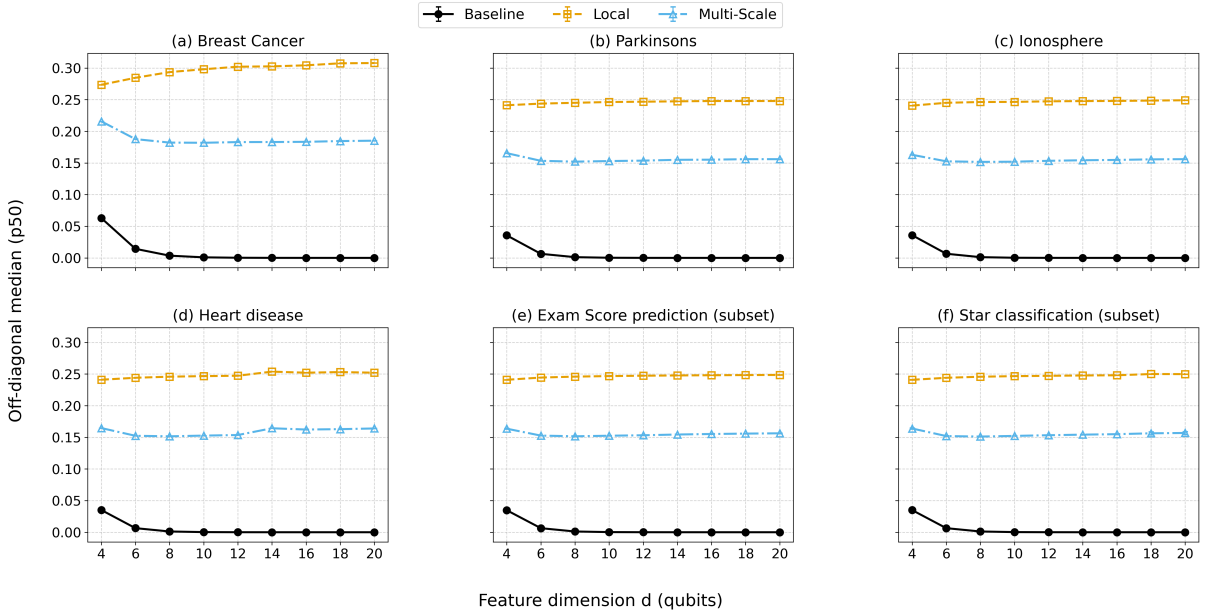


FIG. 1. Off-diagonal concentration (p50) vs. feature dimension  $d$  for all datasets. The baseline fidelity kernel concentrates rapidly as  $d$  increases ( $p50 \rightarrow 0$ ), while the local kernel maintains substantially larger off-diagonal similarities; multi-scale is typically intermediate. All kernels are unit-diagonal normalized.

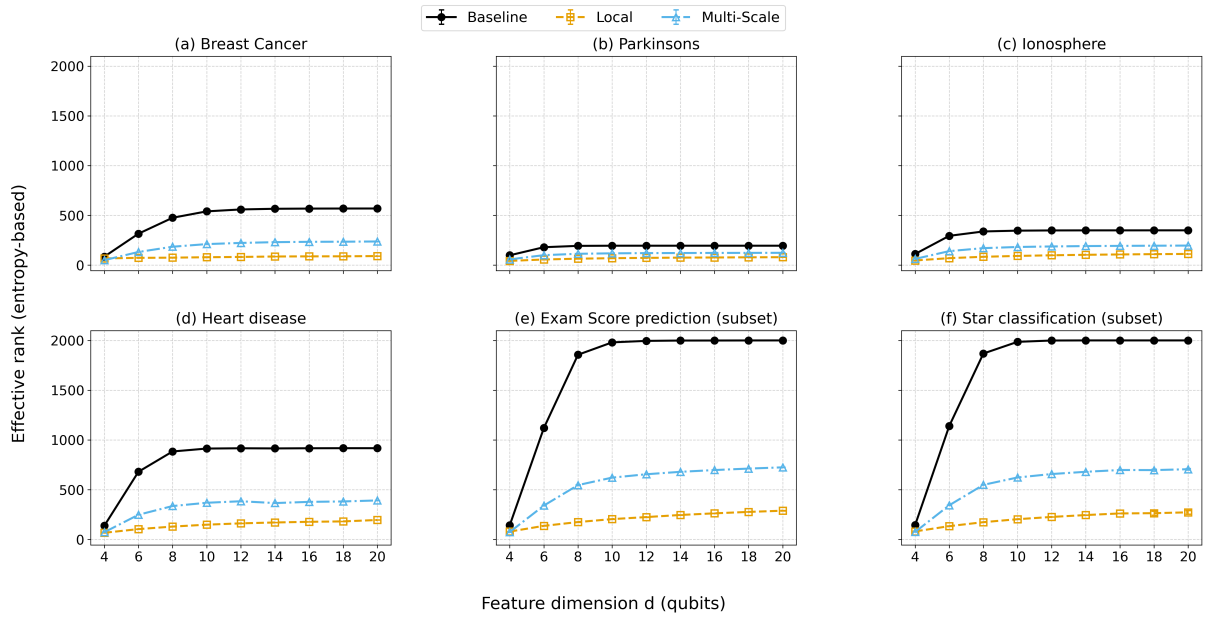


FIG. 2. Entropy-based effective rank  $r_{\text{eff}}(K)$  vs. feature dimension  $d$ . Local kernels generally preserve a richer spectrum (higher effective rank) than the baseline fidelity kernel; multi-scale typically lies between baseline and local.

ing test accuracy. Appendix (Supplementary figures), Sec. C 5 summarizes the validation-selected  $C$  values as a function of  $d$ . This protocol isolates the effect of the kernel while keeping model selection simple and reproducible.

Figure 3 shows test accuracy as a function of  $d$ . Across datasets, we observe that reducing concentration (Section III A) does not necessarily imply improved accuracy: local and multi-scale kernels can match or exceed the baseline on some datasets and dimensions, while remaining compara-

ble or worse on others. This highlights that concentration is a useful diagnostic for kernel geometry, but not a sufficient criterion for predictive performance without additional choices (e.g., patch design, feature map, or depth). Mechanistically, locality and multi-scale mixing change the inductive bias of the similarity measure: while they can mitigate global-state overlap collapse, they can also discard global correlations (or dilute them via averaging) that may be important for a given dataset.

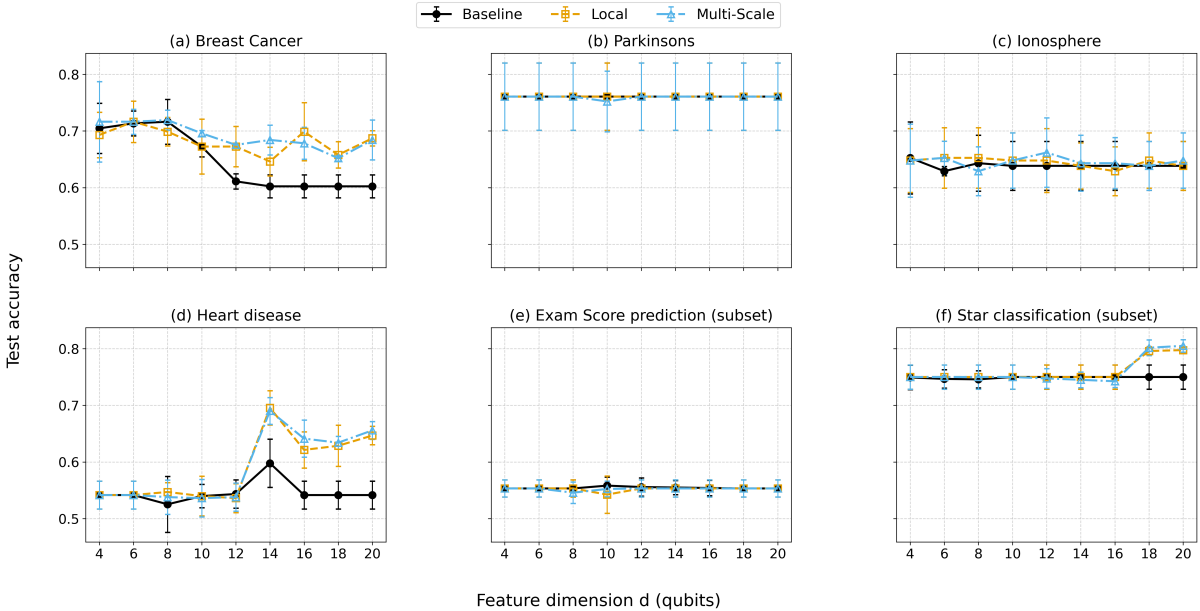


FIG. 3. SVM test accuracy vs. feature dimension  $d$ . For each dataset and  $d$ , the SVM regularization parameter  $C$  is selected by validation accuracy from the fixed grid in Eq. (20), then evaluated once on the test split. Accuracy gains from local and multi-scale kernels are dataset dependent.

### C. Tradeoffs and discussion

The results above show a consistent geometric effect (local and multi-scale constructions mitigate concentration relative to the baseline fidelity kernel), but the performance impact is more nuanced. In particular, reduced concentration does *not* imply higher accuracy in a dataset-independent way.

*a. Reduced concentration does not necessarily imply higher accuracy.* A kernel that is less concentrated (higher off-diagonal p50/p95 and typically higher effective rank) can still fail to improve test accuracy if the preserved variation is not aligned with label structure. Conversely, a more concentrated kernel can remain competitive when the classification task is simple under the chosen encoding, or when regularization compensates for limited similarity variation.

*b. Alignment vs. accuracy.* To bridge geometry and performance, we compute the centered alignment statistic  $\mathcal{A}(K, y)$  (Eq. (19)). While alignment is not a direct proxy for SVM accuracy, it provides a complementary diagnostic: kernels that increase off-diagonal mass but do not improve (or even degrade) alignment can reshape geometry without adding label-relevant structure. Intuitively, centered alignment measures whether variations in  $K$  co-vary with label similarity after removing global mean effects; thus, it is sensitive to whether the additional variability retained by local or multi-scale constructions is plausibly task-relevant rather than merely “less concentrated.”

*c. Computational tradeoffs.* Local and multi-scale kernels reduce concentration by replacing a single global overlap with multiple subsystem-level comparisons, but this typically increases computational overhead. In particular, RDM-based patch kernels require additional partial traces (one per patch

and sample in the simplest implementation), and multi-scale kernels further multiply this cost across scales; these trade-offs motivate the optional Nyström approximation (Section II) when scaling to larger datasets. Intuitively, centered alignment measures whether variations in  $K$  co-vary with label similarity after removing global mean effects; thus, it is sensitive to whether the additional variability retained by local or multi-scale constructions is plausibly task-relevant rather than merely “less concentrated.”

*d. Computational tradeoffs.* Local and multi-scale kernels reduce concentration by replacing a single global overlap with multiple subsystem-level comparisons, but this typically increases computational overhead. In particular, RDM-based patch kernels require additional partial traces (one per patch and sample in the simplest implementation), and multi-scale kernels further multiply this cost across scales; these trade-offs motivate the optional Nyström approximation (Section II) when scaling to larger datasets.

*e. Global view: test-accuracy deltas.* Figure 4 summarizes the test-accuracy change relative to the baseline kernel as a function of dataset and  $d$ . This view makes clear that gains from local and multi-scale kernels are heterogeneous across datasets and across dimensions.

*f. Per-dataset deltas across  $d$ .* To connect the global heatmap view with per-dataset trends, Appendix C (Fig. 7) shows the test accuracy delta relative to baseline as a function of  $d$ .

*g. Tradeoff plots: concentration vs. accuracy.* Finally, Appendix C (Fig. 8) visualizes the empirical relationship between kernel concentration (off-diagonal p50) and test accuracy. Across datasets, these scatter plots illustrate that higher p50 (less concentration) can correlate with accuracy in some cases, but the relationship is not universal. Figure 5 summa-

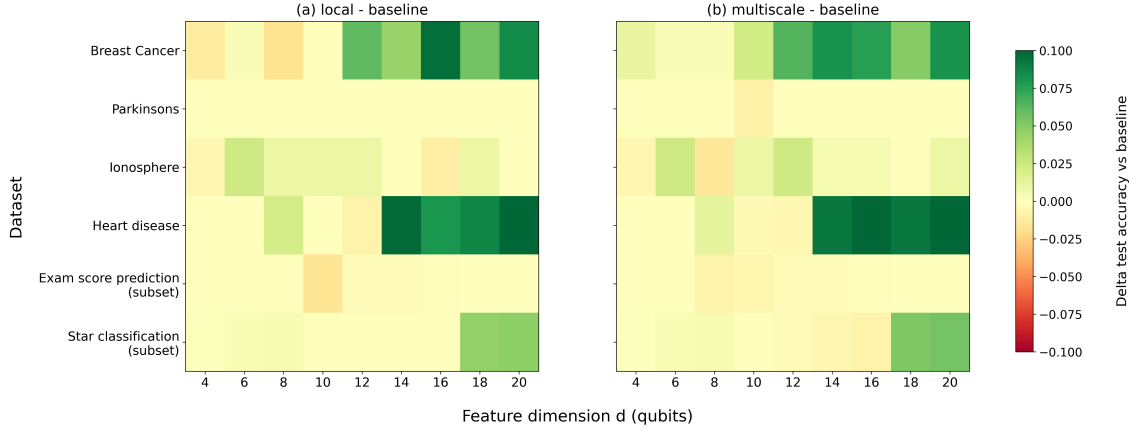


FIG. 4. Heatmaps of test-accuracy deltas relative to baseline across datasets (rows) and feature dimensions  $d$  (columns).

rizes the mean test-accuracy delta relative to baseline for each dataset, averaged across  $d \in \{4, 6, \dots, 20\}$ .

#### IV. CONCLUSION AND OUTLOOK

We investigated two practical strategies to mitigate exponential concentration in fidelity-based quantum kernels: local (patch-wise) constructions that aggregate subsystem similarities and multi-scale mixtures that combine kernels across patch granularities. Across a common sweep in feature dimension  $d \in \{4, 6, \dots, 20\}$  and multiple tabular datasets, both constructions consistently reshaped kernel geometry relative to the global fidelity baseline, yielding larger off-diagonal similarity statistics and a richer spectrum as quantified by the effective rank.

At the same time, the downstream impact on SVM test accuracy was heterogeneous. Reduced concentration improved predictive performance in some regimes but did not provide a dataset-independent guarantee, underscoring that geometric diagnostics (p50/p95, effective rank, and centered alignment) are informative but not sufficient on their own to certify task-relevant similarity.

Several directions remain open. First, patch design and scale weighting could be selected in a data-driven manner (e.g., via validation), subject to constraints that preserve positive semidefiniteness. Second, extending these constructions to shot-based estimation and noisy hardware will require careful treatment of statistical error, error mitigation, and the computational cost of reduced-state estimation. More broadly, locality and scale mixing provide flexible knobs to control kernel concentration while retaining compatibility with classical kernel pipelines, and they offer a practical basis for further

studies of learnability and resource tradeoffs in quantum kernel methods.

#### V. ACKNOWLEDGMENTS

This work was carried out as part of the Qiskit Advocate Mentorship Program (QAMP 2025). All authors participated as Qiskit Advocates on a voluntary basis. We thank the QAMP organizers for coordinating the program and providing a collaborative environment. This work received no external funding. Any opinions, findings, and conclusions expressed in this manuscript are those of the authors and do not necessarily reflect the views of IBM, Qiskit, or the Qiskit community.

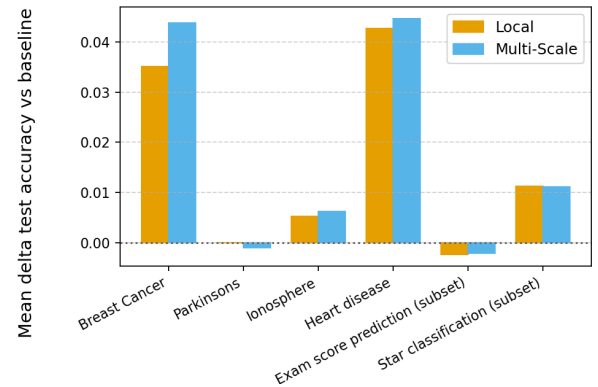


FIG. 5. Mean test-accuracy delta relative to the baseline kernel, reported per dataset and averaged across feature dimensions  $d \in \{4, 6, \dots, 20\}$ . Positive values indicate that the local or multi-scale kernel improves accuracy on average, while negative values indicate a decrease relative to baseline.

[1] Bernhard Schölkopf and Alexander J. Smola. *Learning with Kernels: Support Vector Machines, Regularization, Optimization, and Beyond*. MIT Press, Cambridge, MA, 2002. ISBN 9780262194754.

[2] Maria Schuld, Ryan Sweke, and Johannes Jakob Meyer. Effect of data encoding on the expressive power of variational

quantum-machine-learning models. *Physical Review A*, 103(3): 032430, 2021.

[3] Maria Schuld and Nathan Killoran. Quantum machine learning in feature Hilbert spaces. *Physical Review Letters*, 122(4): 040504, 2019. doi:10.1103/PhysRevLett.122.040504.

[4] Vojtěch Havlíček, Antonio D. Cárcoles, Kristan Temme, Aram W. Harrow, Abhinav Kandala, Jerry M. Chow, and Jay M. Gambetta. Supervised learning with quantum-enhanced feature spaces. *Nature*, 567(7747):209–212, 2019. doi: 10.1038/s41586-019-0980-2.

[5] John Preskill. Quantum computing in the NISQ era and beyond. *Quantum*, 2:79, 2018. doi:10.22331/q-2018-08-06-79.

[6] Jacob Biamonte, Peter Wittek, Nicola Pancotti, Patrick Rebentrost, Nathan Wiebe, and Seth Lloyd. Quantum machine learning. *Nature*, 549(7671):195–202, 2017.

[7] Supanut Thanasilp, Samson Wang, Marco Cerezo, and Zoë Holmes. Exponential concentration in quantum kernel methods. *Nature Communications*, 15:5200, 2024. doi:10.1038/s41467-024-49287-w.

[8] Gabriele Agliardi, Giorgio Cortiana, Anton Dekusar, Kumar Ghosh, Naeimeh Mohseni, Corey O’Meara, Víctor Valls, Kavitha Yogaraj, and Sergiy Zhuk. Mitigating exponential concentration in covariant quantum kernels for subspace and real-world data. *npj Quantum Information*, 12(1):12, 2025. ISSN 2056-6387. doi:10.1038/s41534-025-01154-2. URL <https://doi.org/10.1038/s41534-025-01154-2>.

[9] Utkarsh Singh, Jean-Frédéric Laprade, Aaron Z. Goldberg, and Khabat Heshami. A resource efficient quantum kernel, 2025. URL <https://arxiv.org/abs/2507.03689>.

[10] Hsin-Yuan Huang, Richard Kueng, and John Preskill. Power of data in quantum machine learning. *Nature Communications*, 12:2631, 2021. doi:10.1038/s41467-021-22539-9.

[11] Ali Javadi-Abhari, Matthew Treinish, Kevin Krsulich, Christopher J. Wood, Jake Lishman, Julien Gacon, Simon Martiel, Paul D. Nation, Lev S. Bishop, Andrew W. Cross, Blake R. Johnson, and Jay M. Gambetta. Quantum computing with qiskit, 2024.

[12] Breast cancer wisconsin (diagnostic) dataset (`load_breast_cancer`). scikit-learn dataset loader (`sklearn.datasets`), 2026. URL [https://scikit-learn.org/stable/datasets/toy\\_dataset.html#breast-cancer-wisconsin-diagnostic-dataset](https://scikit-learn.org/stable/datasets/toy_dataset.html#breast-cancer-wisconsin-diagnostic-dataset). Accessed via `sklearn.datasets.load_breast_cancer()`.

[13] Parkinsons dataset (openml data\_id=1488). OpenML via scikit-learn (`sklearn.datasets.fetch_openml`), 2026. URL <https://www.openml.org/d/1488>. Accessed via `sklearn.datasets.fetch_openml(data_id=1488)`.

[14] Ionosphere dataset. Kaggle dataset: jamieleech/ionosphere, 2026. URL <https://www.kaggle.com/datasets/jamieleech/ionosphere>.

[15] Heart disease dataset. UCI Machine Learning Repository (Dataset ID 45), 2026. URL <https://archive.ics.uci.edu/dataset/45/heart+disease>.

[16] Exam score prediction dataset. Kaggle dataset: kundanbedmutha/exam-score-prediction-dataset, 2026. URL <https://www.kaggle.com/datasets/kundanbedmutha/exam-score-prediction-dataset/code>.

[17] Stellar classification dataset (sdss17). Kaggle dataset: fedesoriano/stellar-classification-dataset-sdss17, 2026. URL <https://www.kaggle.com/datasets/fedesoriano/stellar-classification-dataset-sdss17>.

[18] Christopher K. I. Williams and Matthias Seeger. Using the nyström method to speed up kernel machines. In *Advances in Neural Information Processing Systems*, 2001.

[19] Olivier Roy and Martin Vetterli. The effective rank: A measure of effective dimensionality. *Proceedings of the European Signal Processing Conference (EUSIPCO)*, 2007.

[20] Nello Cristianini, John Shawe-Taylor, André Elisseeff, and Jaz Kandola. On kernel-target alignment. In *Advances in Neural Information Processing Systems*, volume 14. MIT Press, 2001.

---

**Appendix A: Local (patch-wise) kernel construction**


---

**Algorithm 1:** Local Quantum Kernel Construction

---

**Input:** Dataset  $X \in \mathbb{R}^{n \times d}$ ; feature map circuit family  $U_\phi(\cdot)$  with depth  $L$ ; patch set  $\mathcal{P} = \{P_1, \dots, P_M\}$  (optional); method  $\in \{\text{SUBCIRCUITS}, \text{RDM}\}$ ; RDM metric  $\in \{\text{FIDELITY}, \text{HS}\}$  (only for RDM); aggregation rule  $\text{AGG} \in \{\text{MEAN}, \text{WEIGHTED}\}$  with optional weights  $\{w_m\}$

**Output:** Kernel matrix  $K \in \mathbb{R}^{n \times n}$

```

1 if  $\mathcal{P}$  is not specified then
2   Define default disjoint adjacent pairs  $P_m = (2m, 2m + 1)$ 
3 if AGG = WEIGHTED then
4   Validate  $w_m \geq 0$  and renormalize so that  $\sum_m w_m = 1$ 
5 Initialize empty list  $\mathcal{G}$ ;
6 if METHOD = SUBCIRCUITS then
7   foreach patch  $P \in \mathcal{P}$  do
8     Construct the patch feature map  $U_\phi^{(P)}(\cdot)$  acting on  $|P|$  qubits;
9     for  $i = 1$  to  $n$  do
10      Form the patch feature subvector  $\mathbf{x}_{i,P}$  by selecting components of  $\mathbf{x}_i$  indexed by  $P$ ;
11      Prepare the patch state  $|\psi_i^{(P)}\rangle = U_\phi^{(P)}(\mathbf{x}_{i,P})|0\rangle^{\otimes|P|}$ ;
12      Compute patch Gram matrix  $G^{(P)}$  with entries  $G_{ij}^{(P)} = |\langle\psi_i^{(P)} | \psi_j^{(P)}\rangle|^2$ ;
13      Append  $G^{(P)}$  to  $\mathcal{G}$ ;
14 else if METHOD = RDM then
15   Construct full feature map  $U_\phi(\cdot)$  on  $d$  qubits;
16   for  $i = 1$  to  $n$  do
17     Prepare full state  $|\psi_i\rangle = U_\phi(\mathbf{x}_i)|0\rangle^{\otimes d}$ ;
18   foreach patch  $P \in \mathcal{P}$  do
19     Let  $\bar{P}$  denote the complement of  $P$  in  $\{0, 1, \dots, d - 1\}$ ;
20     for  $i = 1$  to  $n$  do
21       Compute reduced density matrix  $\rho_i^{(P)} = \text{Tr}_{\bar{P}}(|\psi_i\rangle\langle\psi_i|)$ ;
22       Compute patch Gram matrix  $G^{(P)}$  with entries  $G_{ij}^{(P)} = \begin{cases} 1, & i = j \\ F(\rho_i^{(P)}, \rho_j^{(P)}), & i \neq j \text{ and FIDELITY} \\ \text{Tr}(\rho_i^{(P)} \rho_j^{(P)}), & i \neq j \text{ and HS} \end{cases}$  Append  $G^{(P)}$  to  $\mathcal{G}$ ;
23 Aggregate patch kernels:  $K \leftarrow \text{AGG}(\{G^{(P)}\}_{P \in \mathcal{P}})$ ;
24 Symmetrize  $K \leftarrow (K + K^\top)/2$ ;
25 Normalize  $K$  to unit diagonal:  $K_{ij} \leftarrow \frac{K_{ij}}{\sqrt{K_{ii}K_{jj}}}$ ;
26 Project  $K$  onto the PSD cone via eigenvalue clipping;
27 Renormalize  $K$  to unit diagonal;
28 return  $K$ ;

```

---

## Appendix B: Multi-scale kernel construction

---

**Algorithm 2:** Multi-Scale Quantum Kernel Construction

---

**Input:** Dataset  $X \in \mathbb{R}^{n \times d}$ ; feature map circuit family  $U_\phi(\cdot)$  with depth  $L$ ; scales  $\{\mathcal{P}^{(s)}\}_{s=1}^S$  (optional); scale weights  $\{\alpha_s\}_{s=1}^S$  (optional, nonnegative); normalize flag (default: true)

**Output:** Kernel matrix  $K \in \mathbb{R}^{n \times n}$

```

1 if scales are not specified then
2   Define default scales:
3   (i) disjoint adjacent pairs  $\mathcal{P}^{(1)} = \{(0,1), (2,3), \dots\}$ 
4   (ii) full system  $\mathcal{P}^{(2)} = \{(0,1, \dots, d-1)\}$ 
5 Validate scales (nonempty patches, indices in  $\{0, 1, \dots, d-1\}$ );
6 Renormalize weights so that  $\alpha_s \geq 0$  and  $\sum_{s=1}^S \alpha_s = 1$ ;
7 for  $i = 1$  to  $n$  do
8   Prepare full state  $|\psi_i\rangle = U_\phi(\mathbf{x}_i) |0\rangle^{\otimes d}$ ;
9 Initialize kernel  $K \leftarrow 0_{n \times n}$ ;
10 foreach scale  $s = 1, \dots, S$  do
11   Initialize per-scale kernel  $K^{(s)} \leftarrow 0_{n \times n}$ ;
12   foreach patch  $P \in \mathcal{P}^{(s)}$  do
13     if  $|P| = d$  then
14       for  $i = 1$  to  $n$  do
15         for  $j = i$  to  $n$  do
16            $K_{ij}^{(s)} += |\langle \psi_i | \psi_j \rangle|^2$ ;
17            $K_{ji}^{(s)} += |\langle \psi_i | \psi_j \rangle|^2$ ;
18     else
19       Let  $\bar{P}$  denote the complement of  $P$  in  $\{0, 1, \dots, d-1\}$ ;
20       for  $i = 1$  to  $n$  do
21         Compute reduced density matrix  $\rho_i^{(P)} = \text{Tr}_{\bar{P}}(|\psi_i\rangle \langle \psi_i|)$ ;
22         for  $i = 1$  to  $n$  do
23           for  $j = i$  to  $n$  do
24              $K_{ij}^{(s)} += \text{Tr}(\rho_i^{(P)} \rho_j^{(P)})$ ;
25              $K_{ji}^{(s)} += \text{Tr}(\rho_i^{(P)} \rho_j^{(P)})$ ;
26   Average over patches:  $K^{(s)} \leftarrow \frac{1}{|\mathcal{P}^{(s)}|} K^{(s)}$ ;
27   Accumulate weighted contribution:  $K \leftarrow K + \alpha_s K^{(s)}$ ;
28 Normalize  $K$  to unit diagonal:  $K_{ij} \leftarrow \frac{K_{ij}}{\sqrt{K_{ii} K_{jj}}}$ ;
29 Symmetrize  $K \leftarrow (K + K^\top)/2$ ;
30 return  $K$ ;

```

---

## Appendix C: Supplementary figures

The supplementary figures provide additional detail and alternative views of the main results in Section III. They expand on the concentration diagnostics, spectral structure, and performance trends across datasets and feature dimensions. Specifically, we report (i) the upper-tail off-diagonal concentration statistic p95 (Fig. 6), (ii) per-dataset test-accuracy deltas relative to the baseline kernel as a function of  $d$  (Fig. 7), (iii) tradeoff scatter plots between concentration (p50) and test accuracy (Fig. 8), (iv) representative eigen-spectra at a fixed dimension (Fig. 9), and (v) the SVM regularization parameter selected by validation (Fig. 10). Together, these plots complement the main text by illustrating variability and tradeoffs that are not fully captured by single-number summaries.

### 1. Off-diagonal concentration tail (p95)

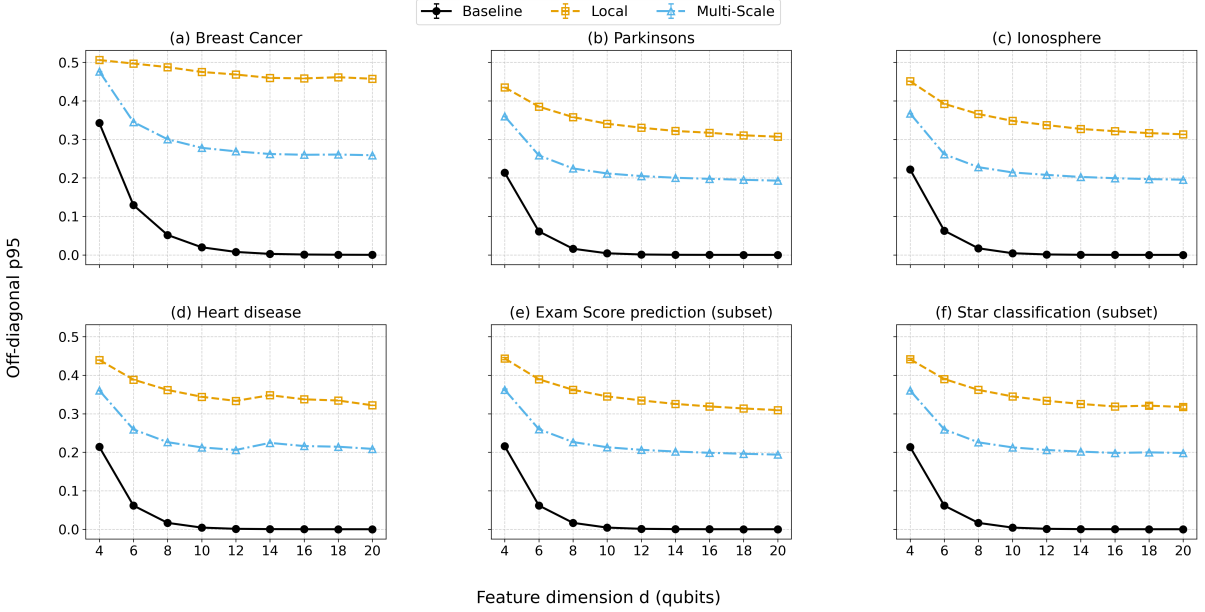


FIG. 6. Off-diagonal concentration tail (p95) vs. feature dimension  $d$ . The same qualitative ordering is observed across datasets: baseline concentrates fastest, local concentrates slowest, and multi-scale is intermediate.

### 2. Per-dataset test-accuracy deltas vs. $d$

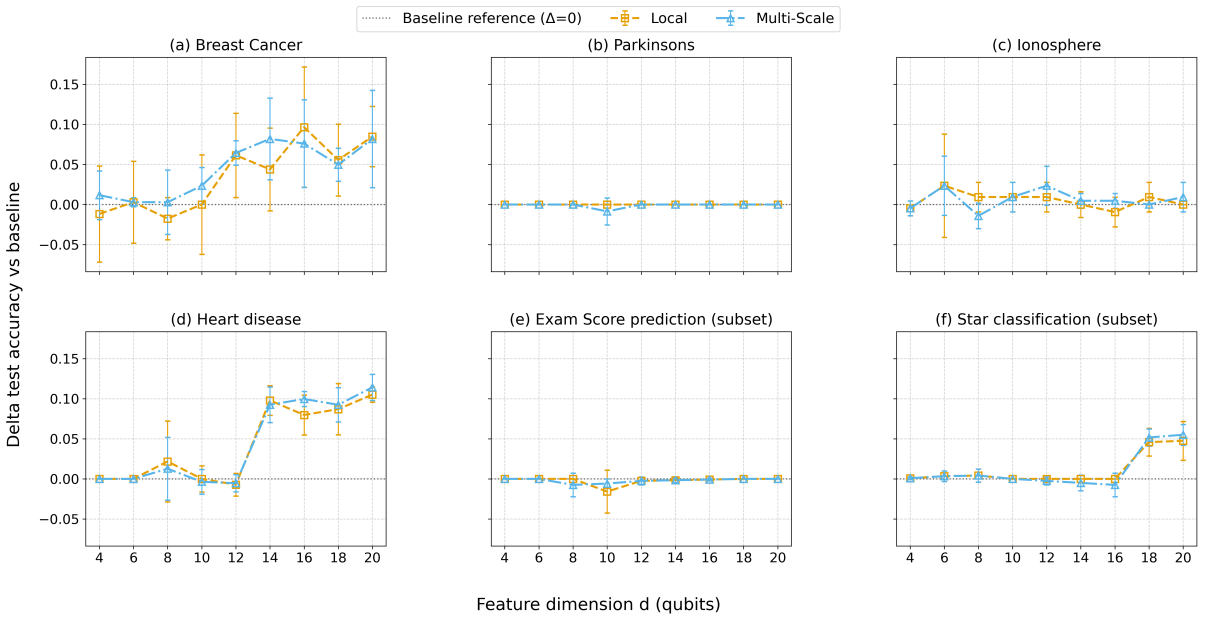


FIG. 7. Test-accuracy delta relative to baseline vs. feature dimension  $d$ . Positive values indicate improvement over the baseline kernel.

### 3. Tradeoff scatter: concentration (p50) vs. test accuracy

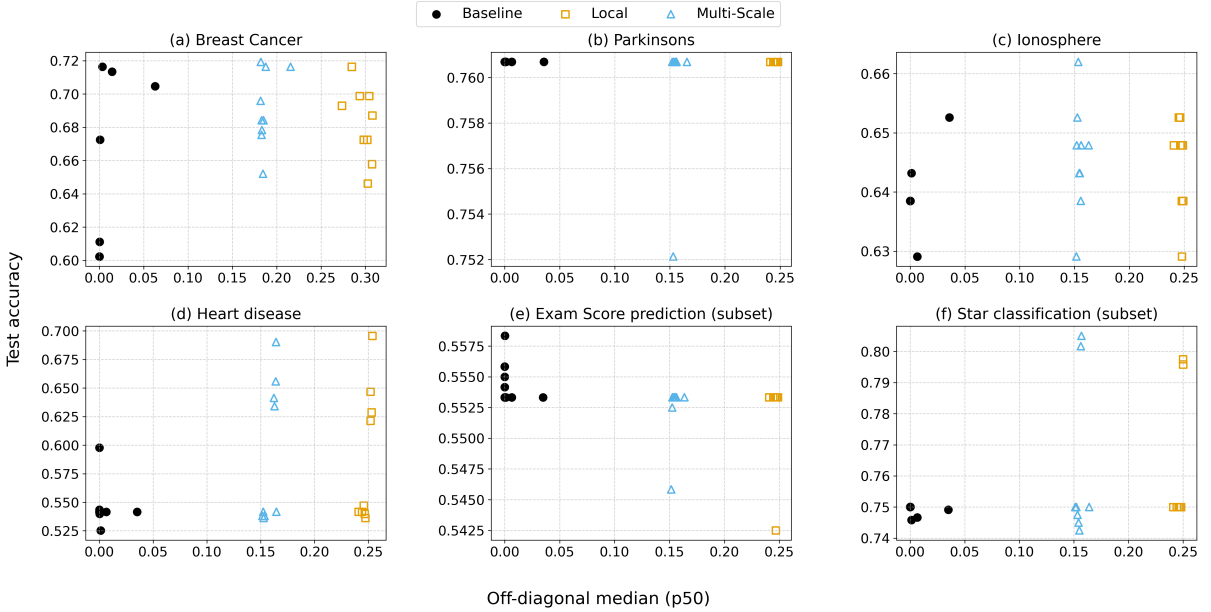


FIG. 8. Tradeoff between off-diagonal concentration (p50) and test accuracy for baseline, local, and multi-scale kernels. These plots highlight that reduced concentration can improve accuracy in some cases, but does not guarantee better performance across all datasets.

### 4. Representative eigen-spectra at $d = 12$

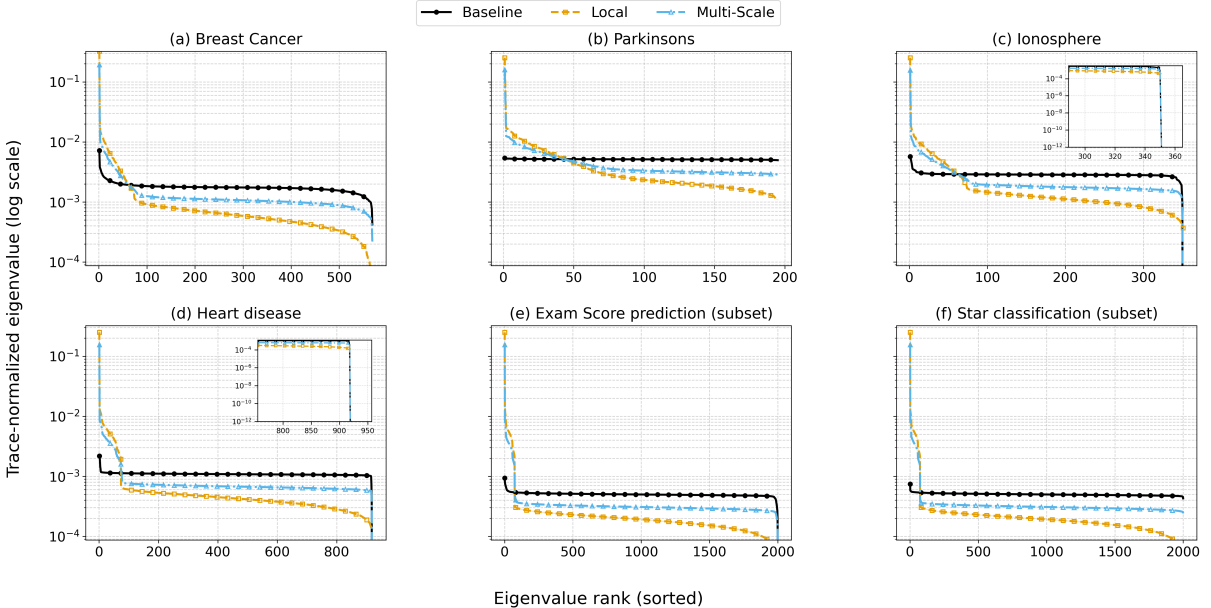


FIG. 9. Representative eigen-spectrum examples at  $d = 12$ . Each panel compares the kernel eigen-spectrum for baseline, local, and multi-scale constructions on the same dataset and dimension. To compare spectral *shape* rather than scale, eigenvalues are normalized by the trace ( $\sum_i \lambda_i$ ) before aggregating across runs, and the vertical axis is shown on a semi-log scale.

### 5. Validation-selected $C$ vs. $d$

Figure 10 reports the value of the SVM regularization parameter  $C$  selected by validation for each dataset and feature dimension  $d$ , for each kernel family. This diagnostic is included to assess the stability of model selection across dimensions and kernels.

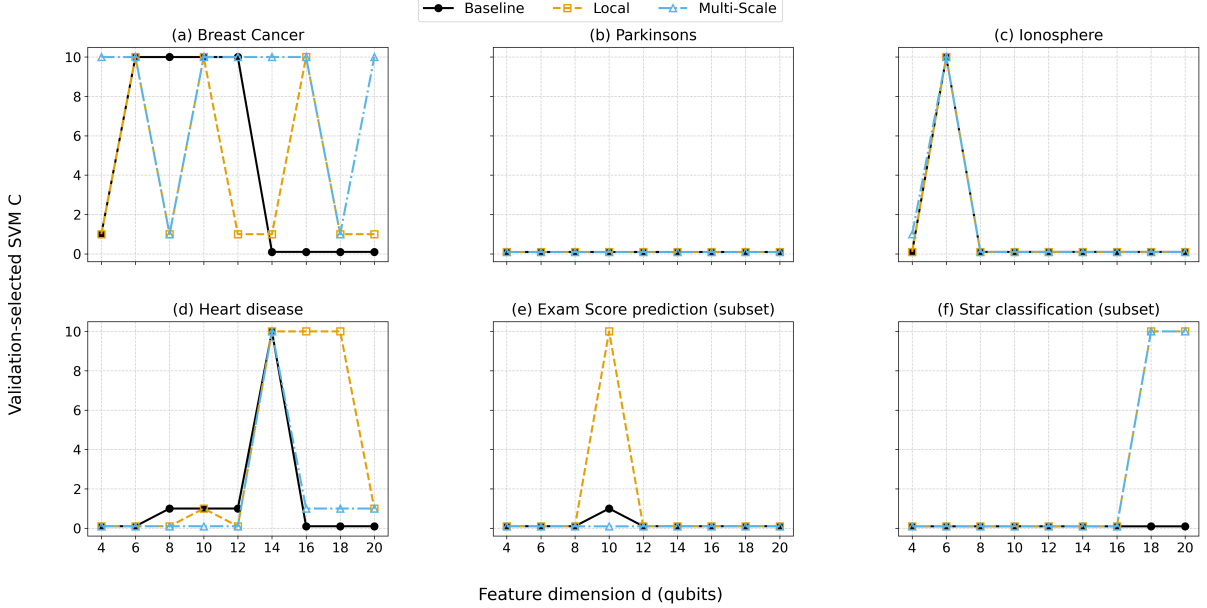


FIG. 10. Validation-selected SVM regularization parameter  $C$  vs. feature dimension  $d$ . For each dataset and  $d$ ,  $C$  is selected from the grid in Eq. (20) independently for each kernel family.